Acta Materialia 229 (2022) 117809

Contents lists available at ScienceDirect

Acta Materialia

journal homepage: www.elsevier.com/locate/actamat

Full length article

Atomistic mechanisms underlying plasticity and crack growth in ceramics: a case study of AlN/TiN superlattices

Nikola Koutná[a,b,*], Lukas Löfler[c,d], David Holec[c], Zhuo Chen[e], Zaoli Zhang[e], Lars Hultman[b], Paul H. Mayrhofer[a], Davide G. Sangiovanni[b]

[a] Institute of Materials Science and Technology, TU Wien, Getreidemarkt 9, Vienna A-1060, Austria
[b] Department of Physics, Chemistry, and Biology (IFM), Linköping University, Linköping SE-58183, Sweden
[c] Department of Materials Science, Montanuniversität Leoben, Franz-Josef-Strasse 18, Leoben A-8700, Austria
[d] Materials Chemistry, RWTH Aachen University, Kopernikusstr. 10, Aachen 52074, Germany
[e] Erich Schmid Institute of Materials Science, Austrian Academy of Sciences, Jahnstrasse 12, Leoben, A-8700, Austria

ARTICLE INFO

Article history:
Received 21 October 2021
Revised 3 February 2022
Accepted 1 March 2022
Available online 4 March 2022

Keywords:
Superlattice
Ceramics
Ab initio molecular dynamics
Deformation
Nanoindentation

ABSTRACT

Interfaces between components of a material govern its mechanical strength and fracture resistance. While a great number of interfaces is present in nanolayered materials, such as superlattices, their fundamental role during mechanical loading lacks understanding. Here we combine ab initio and classical molecular dynamics simulations, nanoindentation, and transmission electron microscopy to reveal atomistic mechanisms underlying plasticity and crack growth in B1 AlN(001)/TiN(001) superlattices under loading. The system is a model for modern refractory ceramics used as protective coatings. The simulations demonstrate an anisotropic response to uniaxial tensile deformation in principal crystallographic directions due to different strain-activated plastic deformation mechanisms. Superlattices strained orthogonal to (001) interfaces show modest plasticity and cleave parallel to AlN/TiN layers. Contrarily, B1-to-B3 or B1-to-B4(B_k) phase transformations in AlN facilitate a remarkable toughness enhancement upon in-plane [110] and [100] tensile elongation, respectively. We verify the predictions experimentally and conclude that strain-induced crack growth—via loss of interface coherency, dislocation-pinning at interfaces, or layer interpenetration followed by formation of slip bands—can be hindered by controlling the thicknesses of the superlattice nanolayered components.

1. Introduction

Protective coatings based on refractory ceramics are hard but typically suffer from brittleness. In particular, tension across a flawed region is a primary cause for crack growth and decohesion. Employing the concept of *superlattice* (SL) architecture [1–6], Hahn *et al.* [7] showed that superior strength and fracture resistance do not have to be mutually exclusive. Varying thicknesses of the SL (semi)coherent nanolayered components, the authors measured a simultaneous hardness and fracture toughness peak for cubic TiN/CrN SL films at bilayer period (Λ) of about 5 nm. While the SL-induced hardness enhancement had already been reported for e.g. TiN/VN [8] or TiN/NbN SLs [9] and explained by hindered dislocation glide within/across interfaces [9,10], Hahn's findings attracted attention to the SL-induced toughening [5,11–13]. To date, however, atomic-level understanding of toughening effects is lacking.

Our model AlN/TiN SL system is a vibrant research topic [1,14–18], especially due to the epitaxial stabilisation of metastable cubic B1-AlN ($Fm\bar{3}m$, *rocksalt*), which is a preferred phase in hard coatings [19–24]. Considerable lattice mismatch of the B1-AlN and B1-TiN ($\approx 4.8\%$ [25]) provides coherency stresses, which inhibit dislocation motion, and thus contribute to hardness enhancement. Specifically, hardness values reported for B1 AlN/TiN SLs reach up to 38 GPa [1,14] and strongly depend on Λ. According to Fallmann *et al.* [14], the hardness peak ($H \approx 37$ GPa) overlaps with the indentation modulus minimum ($E \approx 400$ GPa) measured for films with the lowest bilayer period ($\Lambda \approx 2.5$ nm). The associated H/E ratio, used in the hard coating's community as a phenomenological toughness indicator [26–29], together with cube corner nanoindentation experiments indicate that this SL also has the highest toughness. We note that not only the bilayer period but also AlN-to-TiN volume fraction was varied by Fallmann *et al.* [14], and the

* Corresponding author.
E-mail address: nikola.koutna@tuwien.ac.at (N. Koutná).

https://doi.org/10.1016/j.actamat.2022.117809

most promising SL alternated layers of ≈ 0.9 nm AlN and ≈ 1.5 nm TiN. Generally, the thickness of B1-AlN has a certain limit, which, in turn, limits the hardness enhancement [1]. In case of AlN/TiN SLs, this limit is at least 1.5 nm for films grown on MgO(001) and 0.9 nm for those grown on Si(001) or $Al_2O_3(1\bar{1}02)$ substrates [14,16,30], and it also depends on the interface orientation, as demonstrated for CrN/AlN SL [18]. Increasing AlN layer thickness favours formation of the ground-state hexagonal B4 structure ($P6_3mc$, *wurtzite*). With formation energy slightly above that of the B4 and below that of the B1 phase, the cubic B3-AlN ($F\bar{4}3m$, *zincblende*) is the third frequent polymorph of AlN (see Fig. 2 in Ref. [31]). The B1-AlN forms in SLs with small layer thicknesses, since it provides lower AlN/TiN interfacial energy than the B4 or B3 structures [30,31].

Here, we combine modelling and experimental methods to elucidate atomistic mechanisms underlying strength, plasticity, and crack initiation processes in B1-based AlN/TiN SLs during mechanical loading. Ab initio and classical molecular dynamics simulations allow to gain understanding of mechanical properties over different length scales and to impose well-defined conditions of mechanical load on SLs with sharp interfaces, exact AlN-to-TiN ratio (1:1) and nominal bilayer periods ($\Lambda = \{1.25, 2.5, 5, 10\}$ nm) at a desired temperature (300 K). Main predictions include: (i) modest plasticity orthogonal to interfaces; (ii) greatly enhanced in-plane plasticity (parallel to interfaces) due to strain-mediated B1-to-B3,-B4,-B_k phase transformations; (iii) bilayer-period-controlled extent and distribution of lattice transformations, which governs the SL fracture resistance and overall toughness. Theoretical findings are also qualitatively supported by transmission electron microscopy analyses of AlN/TiN SL films in the as-deposited state and after nanoindentation.

2. Methods

2.1. Computational

Born-Oppenheimer ab initio molecular dynamics (AIMD) calculations were performed using the Vienna Ab-initio Simulation Package (VASP) [32] implemented with projector augmented plane-wave (PAW) pseudopotentials [33] and the generalised gradient approximation [34] for the electronic exchange and correlation effects. The equations of motion were integrated at 1 fs time steps, employing Γ-point sampling of the reciprocal space together with a plane-wave cutoff energy of 300 eV. Total energies at each ionic step were evaluated with accuracy of 10^{-5} eV/supercell.

The cubic (rocksalt) B1 structure constituted the elementary building block of all AlN/TiN supercells, with 576 atoms (288 metal + 288 nitrogen) and total dimensions of $\approx (0.9 \times 1.2 \times 5)$ nm^3. The z vertical axis was aligned with the [001]direction, while the lateral x and y axes were aligned with the $[1\bar{1}0]$ and [110] directions, respectively. SLs with nominal bilayer periods $\Lambda = \{1.25, 2.50, 5.00\}$ nm (prior to relaxation) were designed by populating metallic lattice sites with 144 Al and 144 Ti atoms in a layered manner, keeping the [001] direction orthogonal to interfaces. The computational procedure for modelling tensile deformation followed Refs. [20,35,36]. First, the SL equilibrium structural parameters were optimised using NPT sampling of the configurational space (Parrinello-Rahman barostat [37] and Langevin thermostat set to 300 K). Then, the unstrained supercells (time-averaged stress components $|\sigma_{ii}| \lesssim 0.3$ GPa, $i = x, y, z$) were further equilibrated at 300 K for additional 2 ps in the NVT ensemble (Nosé-Hoover thermostat). Uniaxial tensile loading was simulated by sequentially elongating the supercell in a chosen direction, with strain increments of 2%, while keeping fixed superlattice structural parameters normal to deformation. At each strain step, the structures were rapidly equilibrated by isokinetic velocity rescaling during 300 fs, and subsequently maintained at the same temperature during additional 2.7 ps with the Nosé-Hoover thermostat. Tensile stress in the loaded direction was calculated by averaging the respective stress component for the final 500 fs of each strain step.

The classical molecular dynamics (CMD) calculations were run with the LAMMPS code [38] and a Modified Embedded-Atom Method (MEAM) Al–Ti–N potential developed by Almyras *et al.* [39]. All simulations were performed with a 1 fs time step. CMD superlattice models contained about 250000–300000 atoms, had total dimensions of $\approx (7.6 \times 7.6 \times 40.3)$ nm^3 or $\approx (8.4 \times 7.1 \times 45.0)$ nm^3 and nominal bilayer periods $\Lambda = \{1.25, 2.50, 5.00, 10.00\}$ nm. Similar to the AIMD approach, the supercell structural parameters were first relaxed at 300K, using the isobaric-isothermal (NPT) ensemble coupled to the Nosé-Hoover thermostat. To simulate uniaxial tensile loading, the cells were deformed at each step at a constant rate of 500m/s, with an incremental elongation of 0.005Å. We further note that CMD tensile-testing simulations allowed for lateral Poisson's contraction.

The Supplementary Material describes preliminary AIMD and CMD runs and provides additional analyses complementing those in the main text. Visualisation of selected AIMD and CMD simulation cells and their subsequent analysis was performed with the aid of the OVITO package [40]. Specifically, the function *Coordination analysis* with cut-off radius of 2.4 and 4.8 Å was used to calculate the number of nearest neighbours of Al atoms and the radial distribution function, respectively, the function *Identify diamond structure* [41] was used to evaluate and visualise the total fraction of the B3 and B4 phase, and the function *Dislocation analysis* [42] was used to calculate the lengths and types of dislocations in AlN and TiN layers. See the OVITO documentation for technical details.

Finally, we note that mechanical properties calculated in this work indicate trends for different strain directions or bilayer periods and should always be interpreted on a qualitative level. For example, ideal strength and toughness modulus values (σ_T and U_T, defined in the first subsection of Results and Discussion) represent upper ideal bounds for mechanical performance attainable in real ceramics, which—unlike our supercells—contain native defects, such as dislocations and grain boundaries. Furthermore, the elongation at fracture (ε_F) approximates relative strain that a bulk or a thin-film material may accommodate by local necking at nm length-scale when subject to tension.

2.2. Experimental

The AlN(001)/TiN(001) superlattice thin film (TiN ≈ 1.7 nm, AlN ≈ 0.8 nm) was synthesised by DC unbalanced magnetron sputtering in an AJA International Orion 5 lab-scale deposition system equipped with one three-inch Ti target (Titanium Grade 2) and one two-inch Al target (99.8 at.% purity) from Plansee Composite Materials GmbH. The Ti and Al targets were DC-powered using constant target currents of 1.0 and 0.5 A, respectively. The reactive magnetron sputtering process was carried out at 700° C substrate temperature in an Ar/N_2 mixed gas atmosphere with a flow ratio of 7 sccm / 3 sccm and a total pressure of 0.4 Pa. To ensure a uniform deposition, we used a constant substrate rotation of 1 Hz during film growth. To avoid intermixing of the two-layer materials via excessive ion bombardment, we applied a rather low bias potential of −40 V (floating potential approx. −20 V) to the MgO(001) substrate, just enough to obtain a dense coating morphology. Further details can be found in Ref. [14,43].

The nanoindentation was performed with an Ultra Micro Indentation System (UMIS, Fischer-Cripps Laboratories) equipped with a cube corner diamond tip 100 mN. The maximum load depth was about 1.7 μm. The cross-sectional transmission electron mi-

croscopy (TEM) specimens were prepared using an FEI Quanta 200 3D DBFIB. A 200 kV field emission TEM (JEOL2100F) equipped with an image- side C_S-corrector was used in the high-resolution TEM (HRTEM) study. Based on the images taken from the [001] direction, the quantitative determination of the interplanar spacing was carefully carried out by fitting intensity line profiles using a Gaussian function.

3. Results and discussion

The results of AIMD simulations provide unprecedented atomic-scale understanding of plasticity mechanisms and crack initiation in AlN/TiN SLs subject to load. However, although accurate and reliable, AIMD simulations are limited to predictions within relatively small material domains (≈ 5 nm^3). Thus, we urge the reader to complement AIMD information with the discussion of CMD results. Combined with AIMD, these provide a comprehensive overview of SL mechanical behaviour and fracture mechanisms as a function of Λ up to length scales (≈ 2500 nm^3) observable in experiments (see dedicated sections).

3.1. AIMD stress/strain curves

In our room-temperature AIMD simulations, AlN/TiN SLs with 1:1 AlN-to-TiN ratios and nominal bilayer periods $\Lambda = \{1.25, 2.5, 5\}$ nm were uniaxially strained in three low-index crystallographic directions, orthogonal or parallel to interfaces. Simulations of tensile strain orthogonal to (001) interfaces—along the [001] axis—allow to estimate resistance to decohesion. Contrarily, simulations of tensile strain parallel to interfaces—along the [110] or [100] axis—provide insights for deformation mechanisms active during, e.g., microcantilever bending experiments [44,45] or nanoindentation [1], which locally induce in-plane tensile stresses and may lead to radial (Palmqvist) failure [46]. More generally, these simulations indicate the ability of SLs to laterally redistribute a compression load normal to the surface, thus mimicking the operating conditions typical for protective coatings.

Fig. 1 depicts the stress/strain (σ/ε) curves calculated for different bilayer periods and strain directions. The yield strain (ε_Y, calculated as the point at which the σ/ε slope is $\leq 10\%$ of the initial slope) represents the elastic-response limit and it is associated with the material's yield strength (σ_Y). If the SL deforms plastically, its ultimate tensile strength (σ_T)—which corresponds to the global stress maximum—may be reached at a strain beyond the yield point. Hence, in general, $\sigma_T \geq \sigma_Y$. Finally, the SL fracture strain (ε_F) is associated with the modulus of toughness, U_T, which is the area under the stress/strain curve up to ε_F. In other words, U_T, describes the ability of a material (with no initial cracks) to absorb energy up to fracture, and should be clearly distinguished from the term *fracture toughness*, referring to measurements of conditions causing fracture (stress intensity, K, or strain energy release rate, G) in presence of a crack.

When loaded orthogonal to interfaces (Fig. 1a), AlN/TiN SLs elastically deform up to 12% strain, irrespective of their nominal bilayer period, Λ. The associated yield strengths, $\sigma_Y (= \sigma_T) = 38-39$ GPa, do not show a significant dependence on Λ either. A tensile strain of 14% causes brittle fracture of SLs with Λ of 2.5 and 5 nm, associated with toughness moduli $U_T \approx 3$ GPa. Unlike that, the SL with $\Lambda = 1.25$ nm deforms plastically (atomistic pathways described later) up to $\varepsilon_F = 20\%$ (the fracture strain), leading to improved out-of-plane toughness, $U_T \approx 6$ GPa, in comparison to SLs of larger bilayer periods.

AlN/TiN SLs subject to in-plane (parallel to interfaces) [110] elongation (Fig. 1b) exhibit the same yield strain ($\varepsilon_Y = 12\%$) as observed during [001] tensile testing. The corresponding yield strengths—again nearly invariant of Λ—however, significantly increase up to $\sigma_Y (= \sigma_T) = 49-51$ GPa. Contrarily to simulations for strain normal to interfaces, SLs subject to in-plane [110] elongation display greatly enhanced plasticity, reaching fracture strains $\varepsilon_F \approx 34\%$. The corresponding toughness moduli $U_T \approx 10-11$ GPa exceed those calculated for the [001] loading condition. Although the SL with the lowest bilayer period ($\Lambda = 1.25$ nm) again exhibits the highest ideal tensile toughness ($\approx$11 GPa), the differences in U_T values are relatively small. As shown later, SLs subject to lateral deformations undergo local or extended phase transformations. These structural changes are mirrored by multiple stress minima and maxima in Fig. 1(b).

AIMD simulations indicate that the SL response to in-plane [100] elongation (Fig. 1c) is the softest. Both the initial stress/strain slope ($\equiv$stiffness) in the elastic regime as well as the yield stress are lower than the values calculated for the [001] loading condition. In contrast to results presented in Fig. 1(a,b), however, the ultimate strengths of [100]-elongated SLs are met at strains beyond the yield point ($\varepsilon_Y \approx 10\%$), that is, at 14, 22, and 26% for bilayer period of 1.25, 2.5, and 5 nm, respectively. Therefore, AIMD calculations indicate work strengthening effects for AlN/TiN SLs subject to [100] tensile loading. We emphasise the absence of a clear fracture point in Fig. 1(c) up to 50% elongation (at which the simulation was ended). Hence, the toughness moduli (U_T) obtained via [100] tensile tests reach $\approx$14, $\approx$14, and $\approx$13 GPa for SLs with Λ of 1.25, 2.5, and 5 nm, respectively. These results point towards a remarkable SL ability to activate plastic deformation mechanisms that effectively hinder fracture.

Overall, the calculated AIMD stress/strain curves indicate rather small differences in in-plane tensile strength (σ_T) and tensile toughness (U_T) depending on the SL bilayer period. This may be due to the limited lateral size of our AIMD SL models. Here it is worth noting that CMD simulations (with "large" supercells) indicate an overall superior in-plane toughness for SLs with $\Lambda = 2.5$ nm (discussed later).

The SL strengths $\sigma_T^{[001]} = 38$–39 GPa predicted by our AIMD simulations are essentially equivalent to the AIMD value $\sigma_T^{[001]} = 39$ GPa obtained for B1 $Ti_{0.5}Al_{0.5}N$ solid solutions (see Tab. II in Ref. [20]). However, while mechanical properties of disordered B1 $Ti_{0.5}Al_{0.5}N$ alloys are invariant for symmetry-equivalent lattice directions, our present AIMD results reveal strongly anisotropic mechanical response of nanolayered AlN/TiN SL systems. The most remarkable difference concerns the ability of AlN/TiN SLs to undergo plastic deformation during in-plane tensile strain (Fig. 1b,c) opposed to relative brittleness (or modest plasticity) displayed during elongation orthogonal to interface. These AIMD predictions are supported by "large"-scale CMD simulations (presented later) showing that the observed enhanced in-plane plasticity is not an unphysical artefact of the relatively small lateral sizes of AIMD SL models. In fact, also previous ab initio studies on various B1-based nitride SLs [4,47], including B1 AlN(001)/TiN(001) with Λ between 1.6 and 4 nm [15], pointed towards higher in-plane plasticity as an intrinsic SL-architecture effect. Specifically, a comparison between in-plane and out-of-plane Cauchy pressure (CP) values revealed that $CP_{\parallel} > CP_{\perp}$, which according to Pettifor's phenomenological criterion for ductility [48] indicates greater in-plane than out-of-plane deformability.

3.2. Structural evolution during AIMD tensile tests

To underpin qualitative differences in stress/strain curves for the [001], [110], and [100] loading conditions, as well as to understand effects of the bilayer period on SL plasticity, Figs. 2–4 present snapshots of AlN/TiN SLs at selected strain steps during AIMD simulations. Additional supportive data is shown in the Suppl. Mat. (Fig. S2, Fig. S3).

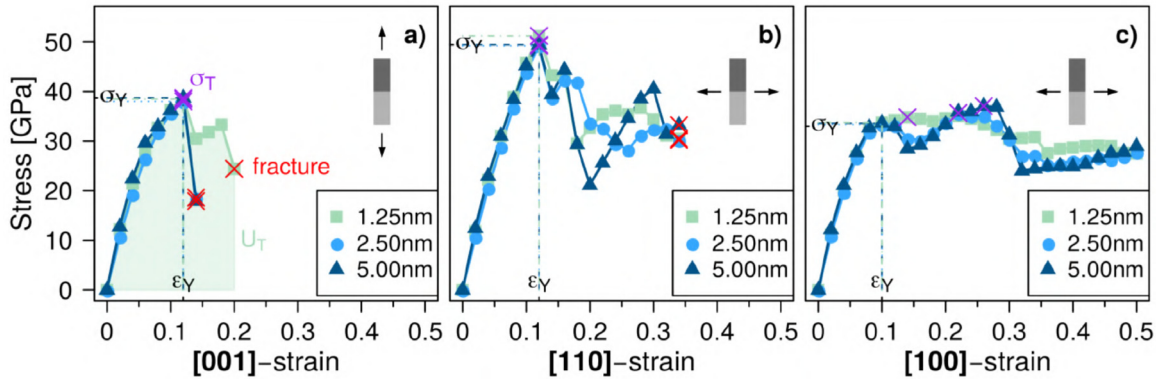

Fig. 1. AIMD stress/strain curves for AlN/TiN SLs subject to uniaxial tensile strain in the (a) [001], (b) [110], or (c) [100] direction. Only the stress component in the loading direction is plotted. The square, circle, and triangle symbols denote nominal bilayer periods of 1.25, 2.5, and 5 nm, respectively. The shaded areas in (a) illustrate the meaning of the toughness modulus (U_T). The purple and red crosses mark the ultimate tensile strength (σ_T) and the fracture point (ε_F), respectively, while the horizontal and vertical lines guide the eye for the yield stress (σ_Y) and strain (ε_Y), respectively.

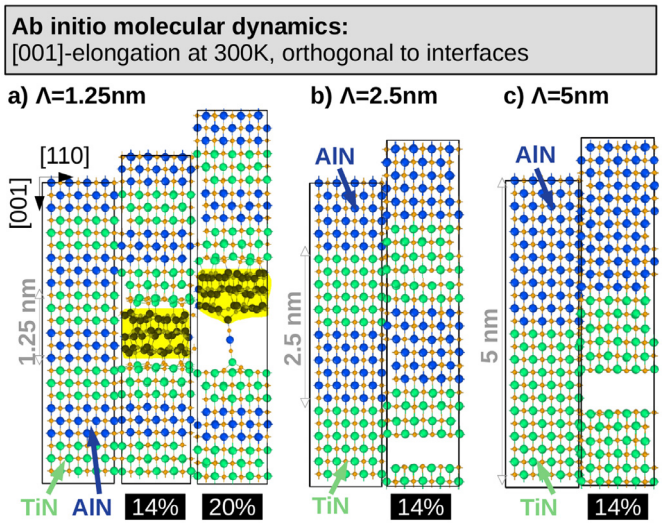

Fig. 2. AIMD snapshots of AlN/TiN SLs with Λ of (a) 1.25 nm, (b) 2.5 nm, and (c) 5 nm, strained in the [001] direction ($\perp$ to interfaces). All snapshots at 14% strain correspond to the stress drop in Fig. 1(a) observed beyond the yield point. The yellow colouring in (a) highlights plastic deformation within the AlN layer, which retards SL fracture until 20% strain. SLs with $\Lambda = \{2.5, 5\}$ nm cleave at 14%, as depicted in (b,c).

When loaded orthogonal to AlN/TiN interfaces (Fig. 2), all SLs cleave in $\approx 90^\circ$ to the applied strain, i.e. parallel to interfaces. As depicted in Fig. 2(a), one AlN layer in the SL with $\Lambda = 1.25$ nm becomes amorphous at $\varepsilon = 14\%$, which is one strain step beyond the yield point ($\varepsilon_Y = 12\%$). This amorphisation—in fact, a partial AlN phase transformation from the B1 to the B4 phase—effectively toughens the SL and retards its fracture, which occurs at 20% strain. In contrast, the SLs with $\Lambda = \{2.5, 5\}$ nm (Fig. 2b,c) show no plasticity and suddenly cleave within TiN layers at 14% [001] strain, directly beyond the yield point. Accordingly, the modulus of toughness predicted for SLs with $\Lambda = \{2.5, 5\}$ nm is smaller than that of the SL with $\Lambda = 1.25$ nm (compare stress/strain areas in Fig. 1(a)). However, the fact that AIMD supercells with $\Lambda = \{2.5, 5\}$ nm contain only one or two independent AlN layers reduces the degrees of freedom for activation of lattice transformations. Indeed, larger-scale CMD simulations presented in the next sections indicate that vertically-strained SLs with different Λ exhibit similar brittleness (low plasticity).

The fact that SLs with $\Lambda = \{2.5, 5\}$ nm break in the middle of the TiN region is perfectly consistent with our previous study [15] modelling brittle cleavage of B1 AlN(001)/TiN(001) SLs by 0 K ab initio calculations. Employing the rigid-block displacement (RBD) method [49], the most inner TiN(001) planes in B1 AlN/TiN SLs with $\Lambda = 2.5$ nm were identified as the easiest cleavage planes for tensile loading orthogonal to interfaces. However, Fig. 2(a) suggests that the occurrence of AlN plastic deformation—not reproducible by the 0 K RBD model—shifts the weakest link in the SL with $\Lambda = 1.25$ nm from TiN to interfaces, likely due to the loss of coherency with the B1-TiN. This observation is later underpinned by CMD results.

Contrarily to [001] AIMD tensile tests, in-plane [110] (Fig. 3) and [100] (Fig. 4) SL deformation does *not* induce brittle cleavage. Instead, SLs undergo different plastic deformation mechanisms, which initiate in AlN layers, break the coherency at AlN/TiN interfaces, and ultimately cause void formation and crack growth (see complementary description of plastic deformation and fracture mechanisms during [110] SL-strain provided by CMD simulations, below).

AIMD snapshots of SLs subject to in-plane [110] strain (Fig. 3) reveal onset of $\{111\}\langle 1\bar{1}0\rangle$ slip in AlN at 14%-strain. Due to the presence of interfaces, however, the process terminates by stacking fault formation (see the yellow colouring at 14%-strain in Fig. 3(a,b,c)). This initiates the B1-to-B3 AlN phase transformation, mirrored by a tensile-stress drop just beyond the SLs yield points (see Fig. 1(b) at 14% strain) and by an increase in shear stress (not shown). The same phase transformation is confirmed by CMD simulations and HRTEM analyses of nanoindented AlN(001)/TiN(001) thin films (presented later). We argue that the hindrance of $\{111\}\langle 1\bar{1}0\rangle$ slip across SL interfaces, with consequent nucleation of stacking faults, is an example of atomistic mechanism responsible for the well-known SL hardening effect.

Fig. 3 further indicates that the extent of the B1-to-B3 AlN transformation above 14%-[110] strain increases with increasing bilayer period Λ. In particular, the entire AlN layer transforms from the B1 to the B3 phase in the SL with $\Lambda = 5$ nm at $\varepsilon = 20\%$ (Fig. 3c). This transformation corresponds to a deep tensile stress minimum in Fig. 1(b) (see dark blue triangle data points at $\varepsilon = 20\%$) and can be rationalised based on the energy variations in pure B1 and B3 AlN under strain. Given the order of lattice parameters: $a_{B3-AlN} > a_{B1-TiN} > a_{B1-AlN}$ [39], an increasing [110]-elongation of AlN(001)/TiN(001) SL monotonically increases strain energy of the B1 building blocks. At the same time, strain energy of a hypothetical B3-AlN polymorph—which would be in compression—progressively diminishes, and eventually becomes lower than that of the B1-AlN. To reduce interfacial misfit with B1-TiN(001) layers, the B1-to-B3 AlN transformation occurs via concerted shear of B1-AlN (111) planes. This leads to the forma-

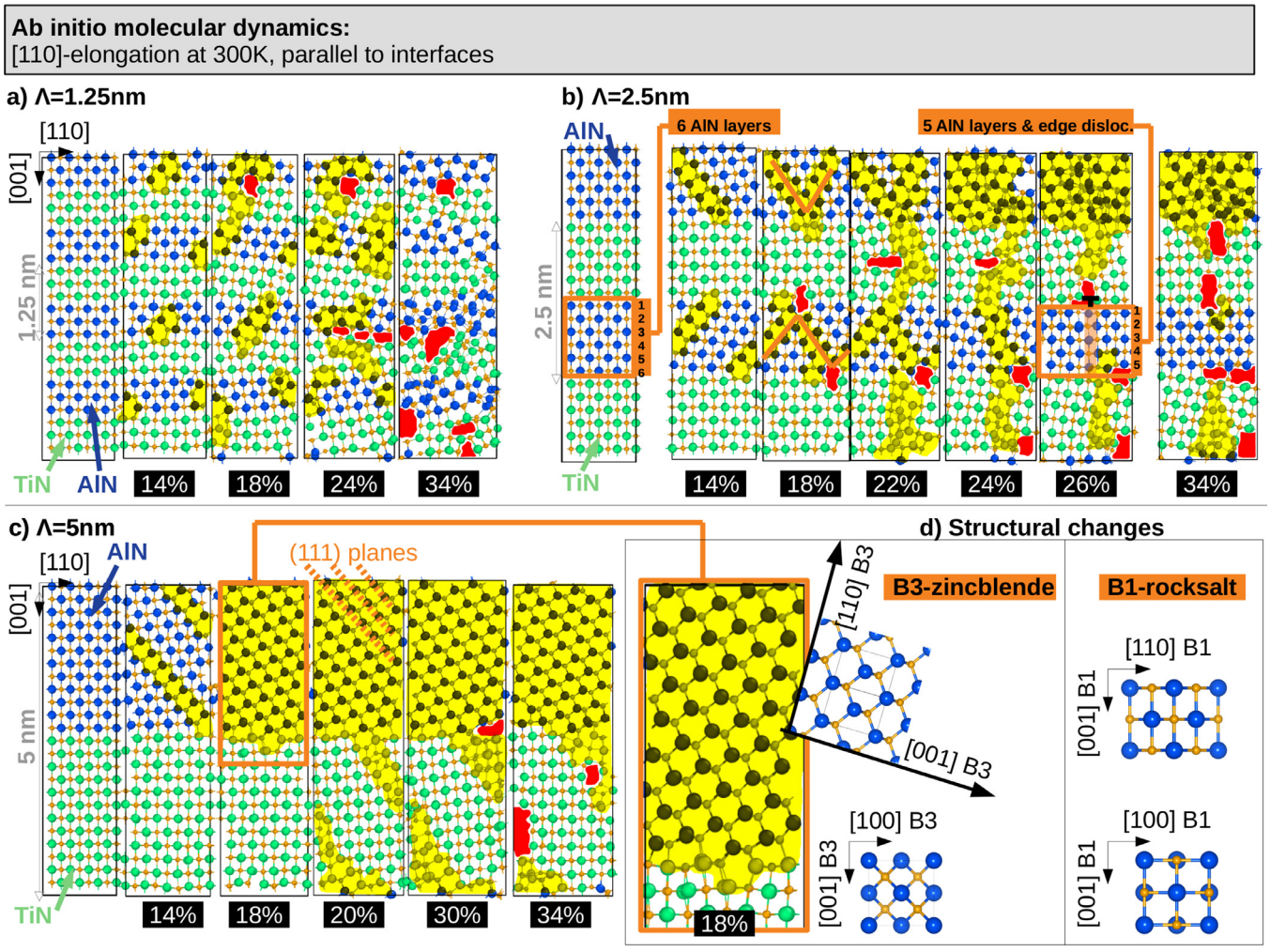

Fig. 3. AIMD snapshots of AlN/TiN SLs with Λ of (a) 1.25 nm, (b) 2.5 nm, and (c) 5 nm, strained in the [110] direction (parallel to interfaces), corresponding to selected strain steps in Fig. 1(b). Snapshots at 14% (a,b,c) correspond to a stress drop one step beyond the yield point. Snapshots at 18% (a), 26% (b), and 20% (c) correspond to the deepest stress minimum during the stage of plastic deformation, while snapshots at 34% (a,b,c) show the fracture point. The yellow colouring highlights structural changes and interface incoherency, while the red colouring marks initiating voids/cracks. Panel (d) illustrates the B1-to-B3 phase transformation in AlN.

tion of a B3-AlN lattice rotated $\approx 33^\circ$ about the $[1\bar{1}0]$ axis. Thus, the [111] axis of B3-AlN is inclined $\approx 33^\circ$ relatively to the [111] direction of the former B1-structure (Fig. 3c,d). With further increase of the [110] strain, the SL incoherency induces bond breakage directly at interfaces or within TiN, as the phase transformation propagates to TiN layers (see red-coloured regions, $\varepsilon > 20\%$, in Fig. 3c). The relatively facile breakage of bonds in TiN is due to the strong preference of this material to retain the B1 phase with 6-fold coordinated atoms (B3 and B4 environments would require 4-fold coordination), as well as to its limited ability to plastically deform [35]. Concerning the SLs with $\Lambda = \{1.25, 2.5\}$ nm, also here the decrease of interface coherency eventually leads to stress accumulation and fracture (see progressive lattice distortion and void formation in Fig. 3a,b).

As discussed above, formation of stacking faults is observed in all SLs at 14% [110]-elongation. Snapshots of the SL with $\Lambda =$ 2.5 nm (Fig. 3b) show two additional stacking faults nucleating in AlN layers at 18% strain, as a consequence of interface-obstructed $\{111\}\langle 1\bar{1}0\rangle$ slip. In each AlN layer, the stacking faults pair up in V- and Λ-shaped defect complexes—shown also later by our CMD simulations—with wedges at SL interfaces (see orange lines in snapshot at $\varepsilon = 18\%$, Fig. 3b). The V- and Λ-shaped defect-pinning on opposite sides of a TiN layer produces local deformation in the TiN bonding network. However, the stress accumulated in the SL is partially dissipated when, at $\varepsilon = 24$–26%, the Λ-shaped defect-pair annihilates via $\frac{1}{2}\{111\}\langle 1\bar{1}0\rangle$ slip (see local stress minimum in Fig. 1b). Annihilation of the defect-pair is followed by a formation of edge dislocation, as highlighted by the orange-shaded area in Fig. 3(b). Consequently, the bottom AlN layer of Fig. 3(b) becomes again fully B1-structured, but with an extra AlN(110) and one less AlN(001) atomic plane (see orange frame in Fig. 3(b) at $\varepsilon = 26\%$). Conversely, the top AlN layer "amorphises" in B3-like local environments. The lattice mismatch due to the edge dislocation and AlN amorphisation induces interfacial strain, thus causing AlN–TiN decohesion and formation of voids within TiN. A similar mechanism for crack initiation is underlined later by CMD simulations.

Comparably to [110] tensile tests, also in-plane [100] elongation (Fig. 4) induces local amorphisation and phase transformations in AlN layers. These structural changes initiate at $\varepsilon = 14$–18%, progressively reduce interface coherency, and may ultimately lead to void growth in TiN. Subject to [100] elongation, however, the B1-AlN phase predominantly transforms towards its hexagonal B4 or hexagonal B_k variants (#194, $P6_3/mmc$ [50,51]). We note that the energetic stability of the B_k polymorph is intermediate to that of B1-AlN and the ground-state B4-AlN [51]. Gradual AlN phase transitions (which also induce transformations in TiN layers for large SL strain (Fig. 4)) are manifested by slow stress variations in the plastic-response range and translate in less pronounced tensile

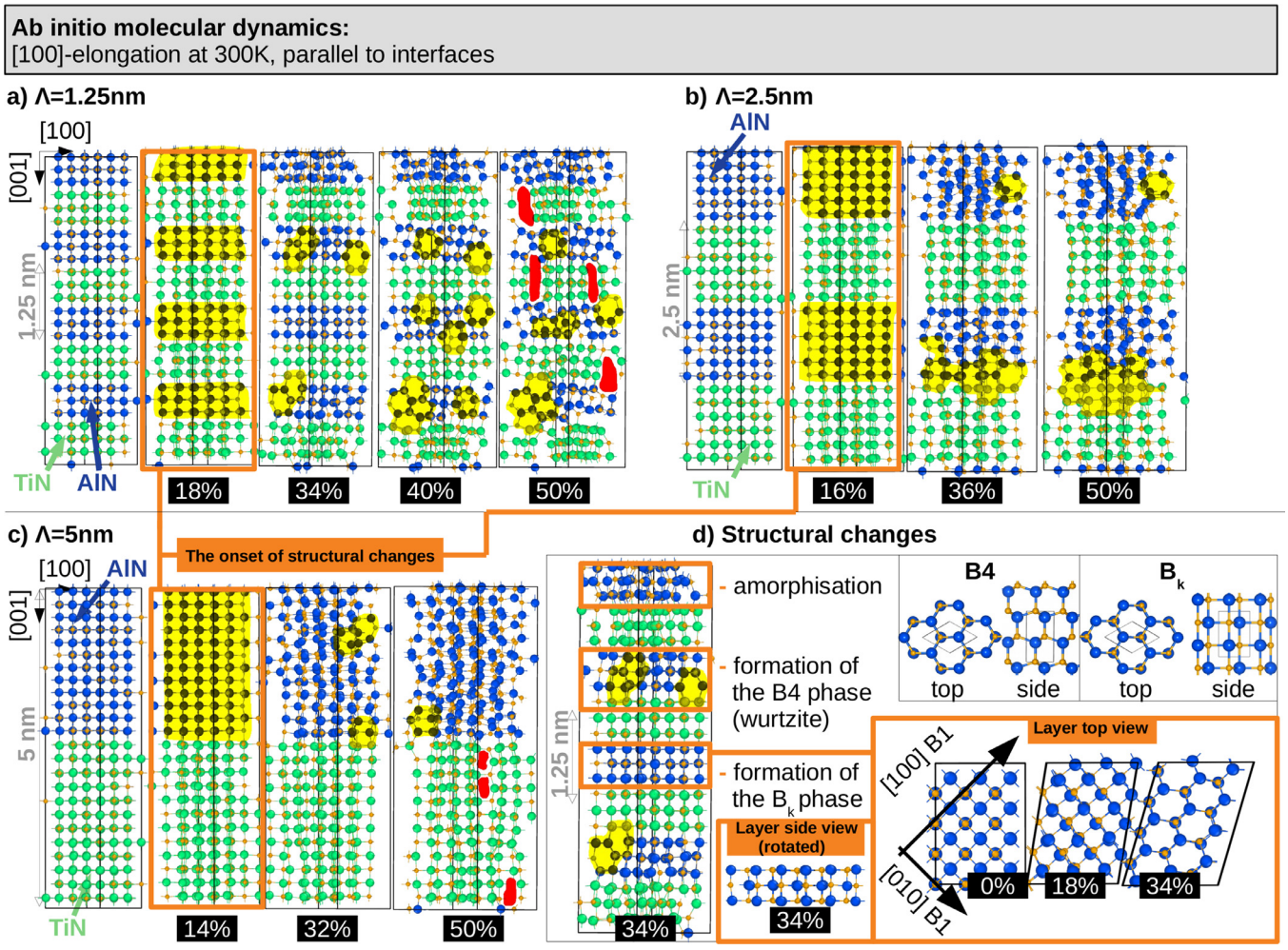

Fig. 4. AIMD snapshots of AlN/TiN SLs with Λ of (a) 1.25 nm, (b) 2.5 nm, and (c) 5 nm, strained in the [100] direction (parallel to interfaces), corresponding to selected strain steps in Fig. 1(c). Snapshots at 18% (a), 16% (b), and 14% (c) correspond to the first local stress minimum beyond the yield point, while snapshots at 50% show the last step of the simulation. The yellow colouring highlights structural changes and interface incoherency, while the red colouring marks initiating voids/cracks. Panel (d) illustrates amorphisation and the B1-to-B4(B$_k$) phase transformation in AlN. We note that due to the same supercell orientation in all AIMD simulations, [100]-elongation was modelled by deforming the lattice diagonally in-plane, as depicted in (d) "Layer top view", while assuring the orthogonality with the [010] direction.

stress minima in Fig. 1(c) in comparison to Fig. 1(b). Similarly to the B3 phase, also the B4 phase—locally stabilised in AlN layers—can re-orient in order to accommodate misfit with TiN, although we observe no collective rotation as in the case of the [110] tensile testing. Based on higher tensile toughness moduli predicted for SLs subject to [100]-elongation compared to [110]-elongation ($U_T^{[100]} = 13 - 14$ GPa, $U_T^{[110]} = 10 - 11$ GPa), we suggest that intermediate (rather than full) phase transformations in AlN layers hinder crack initiation and propagation more effectively.

Our prediction that [001] and [100] tensile strain predominantly trigger the B1-to-B4 transition, while [110] loading favours the B1-to-B3 transition perfectly agrees with previous ab initio calculations by Zhang *et al.* [52,53], although the authors modelled the opposite transformation pathways: B4-to-B1 [52] and B3-to-B1 [53]. In addition to the uniaxial strain path, Refs. [52,53] also described a pure shear transformation path. Furthermore, our predictions are consistent with room-temperature AIMD simulations by Sangiovanni *et al.* [20] that indicated formation of tetrahedrally-coordinated (Al,Ti,N) networks and B4-like environments in B1-$Al_{1-x}Ti_xN$ alloys strained in the [001]-direction. Although not directly related to present findings, we should mention that, as shown by Li *et al.* [17] for the case of fcc-Al(111)/B3-AlN(111) multilayered thin films, coherency strains at interfaces can induce also the reversible B4-to-B3 phase transformation, governed by a collective glide of Shockley partial dislocations on B3-AlN {111} planes.

3.3. Fracture mechanisms from CMD tensile tests

To support and complement AIMD predictions on strain-mediated structural transformations and crack growth mechanisms, we carry out "large"-scale CMD simulations employing a semi-empirical potential by Almyras *et al.* [39], parameterised and validated for elastic, structural, and thermodynamic properties of binary and pseudobinary Ti–Al–N systems. Although semi-empirical potential models generally offer modest accuracy in comparison to ab initio methods, their efficiency allows to overcome limitations of small supercells. Here, CMD simulations are important to achieve detailed atomistic descriptions of SL plasticity and fracture resistance. To underpin bilayer-period-related trends in strength and toughness, additionally to SLs with $\Lambda = \{1.25, 2.5, 5\}$ nm, a SL with $\Lambda = 10$ nm is investigated by CMD (although B1-AlN layer thicknesses above 5 nm are most likely unattainable by epitaxial SL growth in experimental conditions [18]).

Snapshots of CMD tensile tests in Fig. 5 confirm lattice transformation pathways, and complement failure mechanisms, predicted by AIMD. Nonetheless, in comparison to AIMD results (Fig. 1),

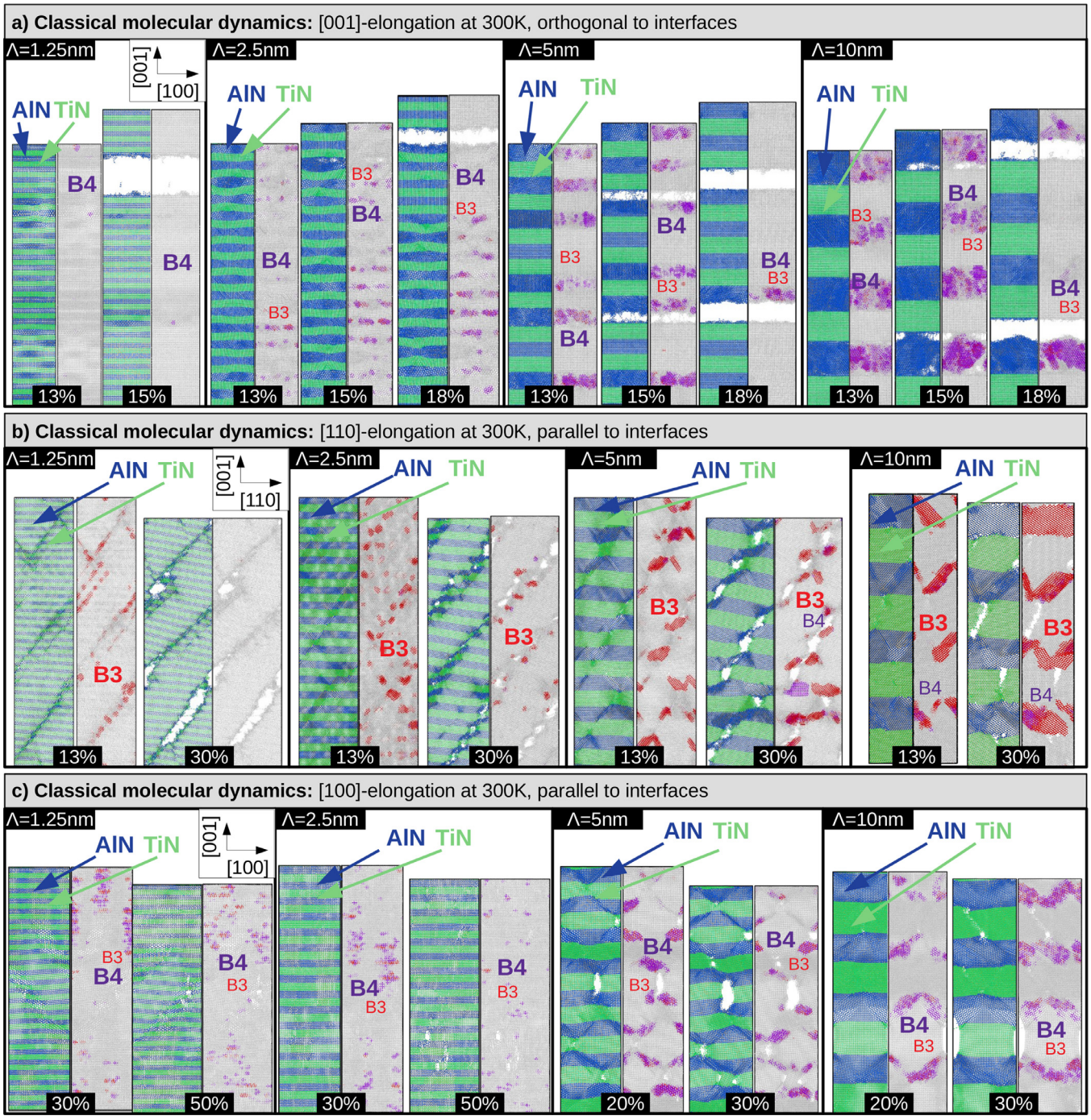

Fig. 5. CMD snapshots of AlN/TiN SLs with $\Lambda = \{1.25, 2.5, 5, 10\}$ nm subject to (a) [001], (b) [110], (c) [100] tensile strain. The red-purple-grey colour code shows regions, where the B3 (red), B4/B_k (purple), or B1/other (grey) structure types are stabilised, as evaluated by the OVITO package [40,41].

CMD stress-strain curves (Fig. S1 in the Suppl. Mat.) exhibit lower stresses and different features. This is mainly due to Poisson's contraction allowed in CMD (vs. lateral supercell size fixed in AIMD) and "large" size of CMD supercells promoting plastic deformation and "earlier" SL yielding. Note also that the potential parameters had not been optimised to materials responses beyond the elastic range.

Consistently with AIMD, AlN/TiN SLs subject to out-of-plane [001] elongation (Fig. 5a) cleave parallel to interfaces at relatively low strains (≈ 15–18%). Cleavage is preceded by local B1-to-B4 (or B_k) AlN transformations (see purple-coloured regions in Fig. 5a), indicated also by AIMD for the SL with $\Lambda = 1.25$ nm. Generally, lattice transformations initiate in one or a few AlN layers, which could explain why AIMD SLs with $\Lambda = \{2.5, 5\}$ nm—having only 2 and 1 AlN layer(s), respectively—exhibit no plasticity and brittle fracture. The overall extent of these transformations increases with increasing bilayer period. An additional result not indicated by "small" AIMD supercells is that stress release after SL fracture facilitates the reverse B4-to-B1 transformation.

Concerning [110] CMD tensile tests (Fig. 5b), SL fracture is observed at elongations approximately twice those reached during [001] loading. Hence, consistently with AIMD, also CMD points towards a greatly enhanced in-plane plasticity. Unlike AIMD, CMD stress-strain curves (Fig. S1b in the Suppl. Mat.) also indicate strain

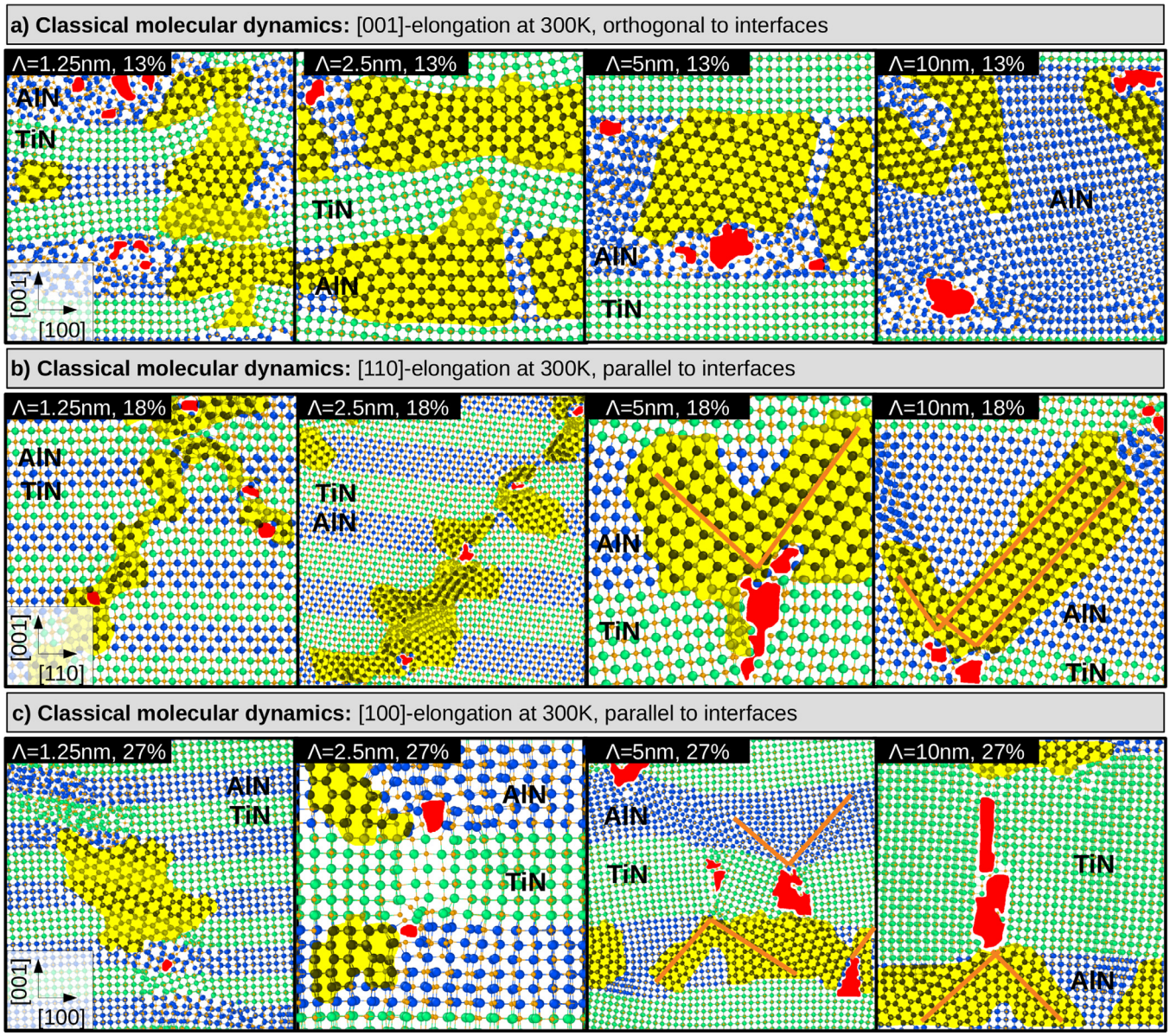

Fig. 6. Local magnifications of CMD AlN/TiN simulation cells (≈ 1 nm thick slices of few SL layers) at selected strain steps during (a) [001], (b) [110], and (c) [100] tensile tests. The yellow colouring highlights structural changes and interface incoherency, the red colouring marks voids/cracks, and the orange lines guide the eye for V- and Λ-shaped defect-pinning on TiN layers. See also Supplementary figures S4–S7.

hardening, manifested as tensile stress maximum beyond the elastic range.

CMD simulations confirm that the B1-to-B3 AlN phase transition initiates via $\{111\}\langle 1\bar{1}0\rangle$ slip, which differs from the most typical $\{110\}\langle 1\bar{1}0\rangle$ slip system operating in monolithic TiN layers at room temperature [54,55]. The B3 domains nucleate in several consecutive AlN layers (see red-coloured regions in Fig. 5b), and, with increasing strain (>13%), develop into shear bands that extend diagonally across the entire SL model. The slip-induced interpenetration of TiN and AlN layers (clearly shown for SLs with $\Lambda = \{1.25, 2.5, 5\}$ nm in Fig. 5b) eventually causes growth of nanocracks inclined $\approx 45^\circ$ to interfaces. This is later confirmed by experimental results.

The notion of superior in-plane plasticity is further underpinned by CMD simulations of SLs subject to [100] tensile elongation (Fig. 5c). In particular, AlN/TiN nanolayers with $\Lambda = \{1.25, 2.5\}$ nm yield fracture strains as high as 50%, which agrees well with AIMD predictions. Consistently with AIMD, the predominant AlN transformation triggered by [100] strain is the B1-to-B4 (B_k). Importantly, however, CMD results show that extent and distribution of structural changes (observed to control the SL resistance to fracture (see below)) vary with Λ.

To further shed light on crack growth mechanisms at atomic level, Fig. 6 presents local magnifications of CMD simulation cells (≈ 1 nm thick slices of few SL layers). Snapshots of SLs elongated orthogonal to interfaces (Fig. 6a) illustrate crack growth due to (i) propagation of the B1-to-B4 transformation to TiN layers, followed by layer shearing ($\Lambda = \{1.25, 2.5\}$ nm), or due to (ii) large incoherencies within AlN layers themselves ($\Lambda = \{5, 10\}$ nm), as a consequence of co-existing B1, B_k, B_4, and amorphous domains.

Fig. 6b illustrates nucleation of B3-AlN environments in SLs subject to [110]-elongation. These often form as V(or Λ-) shaped defect complexes, with wedges at SL interfaces (see orange lines in Fig. 6b, and also Fig. S4 and S5 in the Suppl. Mat.), that induce

local deformations in the TiN bonding network. Irrespective of the bilayer period, formation of V(or Λ-) shaped defects takes place via local rotation and distortion in the AlN sublattice with respect to the host B1 lattice. To release the accumulated shear stresses upon further [110]-elongation, these locally transformed regions grow diagonally across TiN layers and merge into shear bands, eventually causing fracture (Fig. 5b at 30% elongation). SLs with low bilayer periods ($\Lambda = \{1.25, 2.5\}$ nm) are seen to undergo AlN↔TiN layer interpenetration already at strain of 18% (Fig. 6b). A further increase in strain, however, induces shear-mediated layer interpenetration, followed by fracture along the shear lines, in all SLs (including $\Lambda = \{5, 10\}$ nm, see Fig. 5b). Additional view of shear-induced plastic deformation and fracture in SLs subject to [110]-elongation is provided by Figs. S4 and S5.

Formation and pinning of V(or Λ-) shaped defect complexes at interfaces is observed also for [100]-elongated SLs (Fig. 6c), although now the transformed regions primarily consist of B4(B_k)-like AlN. At the onset of local AlN transformations, SLs with higher bilayer periods ($\Lambda = \{5, 10\}$ nm) maintain interfacial coherency (see Suppl. Fig. S7). Ti-N bonds adjacent to interfaces, however, become locally stretched, which enhances AlN/TiN interfacial strain and—upon further increase of [100]-strain—leads to breaking of [100]Ti-N bonds and opening of nanocracks across the TiN layer. In contrast, SLs with lower bilayer periods ($\Lambda = \{1.25, 2.5\}$ nm, for illustration see also Suppl. Fig. S6) subject to [100] strain are observed to reduce accumulated stress via either ($\Lambda = 1.25$ nm): nucleation of B4 domains in AlN, which later grow through both AlN and TiN layers, or ($\Lambda = 2.5$ nm): concerted B1-to-B_k transformation in both TiN and AlN layers, which is also observed in AIMD simulations (Fig. 4). Lattice transformations that extend across both AlN and TiN layers allow considerably delaying fracture in SLs with "low" bilayer periods due to effective redistribution of internal stresses. The differences in structural transformations induced by [100] strain in SLs with "low" (Suppl. Fig. S6) vs. "high" (Suppl. Fig. S7) bilayer periods are interpreted as follows. For the case of "low" Λ, structural transitions extending to TiN layers are possible because B1-to-B4(B_k) transformation of a "thin" portion of TiN is less energetically costly than an increase in B4-AlN/B1-TiN interfacial strain. Conversely, for the case of ($\Lambda = \{5, 10\}$ nm), our results suggest that an increase in B4-AlN/B1-TiN interfacial strain is less energetically costly than transformation of a "thick" TiN region.

3.4. Experimental investigations

The reliability of our computational predictions is supported by high resolution transmission electron microscopy (HRTEM) and nanoindentation testing of magnetron-sputtered AlN(001)/TiN(001) SL films grown on a MgO(001) substrate. The as-deposited films are B1-structured, with bilayer period of 2.5 nm (AlN ≈ 0.9 nm, TiN ≈ 1.6 nm), fully coherent stress state, and a very low misfit dislocation density. The indentation hardness, H, (Berkovich diamond tip) and elastic modulus, E, reach (37.0±0.5) GPa and (397±12) GPa, respectively, while the commonly reported values for TiN_x films range between 20–30 GPa (H) and 330 – 450 GPa (E), see Refs. [11,56,57].

Fig. 7 depicts cross-sectional HRTEM image of AlN/TiN SL film in the as-deposited state and after cube corner indentation, during which penetration of a diamond tip induces predominantly compressive stresses orthogonal to interfaces and a mixture of tensile and shear stresses parallel to interfaces (i.e. sideways from the indentor). While such loading condition clearly differs from the modelled uniaxial elongation, the locally induced in-plane tensile strains are expected to lead to similar transformations and failure mechanisms as simulated during [110] and [100] SL loading.

For the as-deposited SL (Fig. 7a,b), the measured d_{002} interplanar spacings in AlN and TiN layers fall within 1.94–2.03 Å and 2.05–2.23 Å, respectively. These correspond to out-of-plane lattice parameters $a_{AlN} = 3.97 \pm 0.09$ Å and $a_{TiN} = 4.28 \pm 0.18$ Å, consistent with values reported for the parent binary structures: $a_{B1-AlN} = 4.01$–4.07 Å [58–60] and $a_{B1-TiN} = 4.24$–4.26 Å [61,62]. Slight deviations of d_{002} SL values relatively to interatomic distances in binary B1 phases are expected because of Poisson's contraction of AlN layers and expansion of TiN layers along the growth direction (i.e., in-plane tension in AlN vs. compression in TiN layers).

A low-magnification TEM bright-field image (Fig. 7c) shows an overview morphology of the indented SL film, indicating the location of HRTEM observations (Fig. 7d) magnified in Fig. 7e. Quantitatived_{002} measurements (Fig. 7f and Fig. S9 in the Suppl. Mat.) yield $d_{002}^{AlN} = (2.18 \pm 0.05)$ Å and $d_{002}^{TiN} = (2.08 \pm 0.06)$ Å. The resulting lattice parameter $a_{AlN} = (4.35 \pm 0.05)$ Å largely exceeds values foreseeable for B1-AlN, while corresponds well to the range

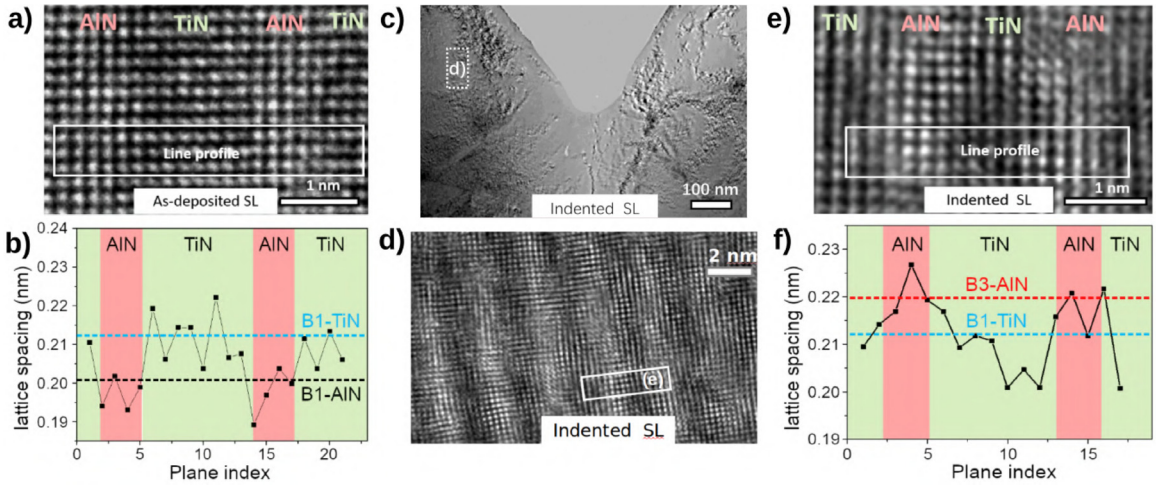

Fig. 7. (a) Cross-sectional HRTEM image of the as-deposited TiN/AlN SL film together with (b) the measured d_{002} lattice spacing variations along the growth direction. (c) A TEM bright-field overview image of the indented film, showing a region close to the indented impression where a cross-sectional HRTEM image was recorded (d). (e) Enlarged HRTEM image used for quantitative analysis of lattice spacings in the indented film (f). Additional data is presented in the Suppl. Mat. (Fig. S9). White boxes in (a) and (e) show the line profile positions, while the dashed horizontal lines in (b) and (f) indicate reference lattice-parameter values for bulk B1-TiN [25], B1-AlN [52], and B3-AlN [52]. Note that for the as-deposited sample (b), the d_{002} expansion in the growth direction is as expected for coherent interfaces, since lattice planes across interfaces must expand for AlN ($a_{B1-AlN} < a_{B1-TiN}$), thus contracting in-plane for AlN due to Poisson's effect.

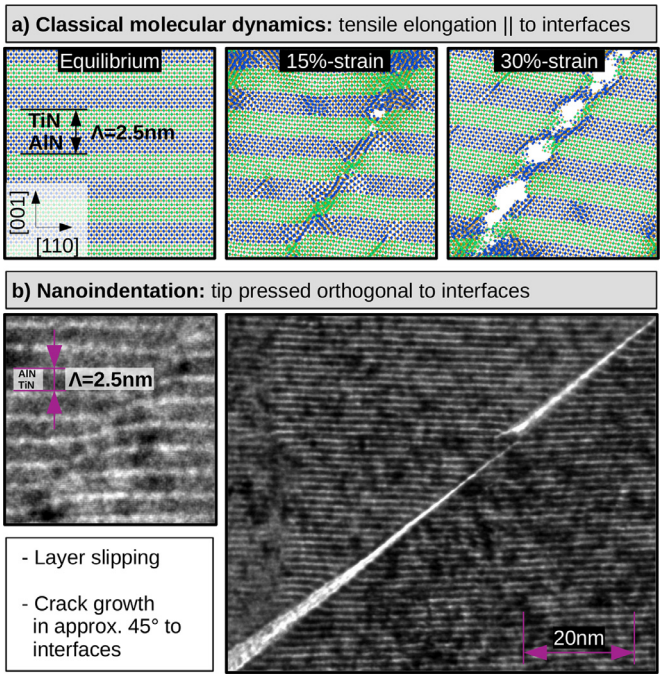

Fig. 8. (a) CMD snapshots of [110]-strain-induced layer slipping and crack growth in AlN/TiN SLs. (b) HRTEM images of nanoindented AlN/TiN SL coatings, indicating similar crack growth in $\approx 45^{\circ}$ to interfaces. Note that the AlN-to-TiN ratio in the experimental SLs is $\approx 1:3$, i.e. different from 1:1 used in our simulations.

of values 4.37–4.39 Å reported for B3-AlN [63,64]. HRTEM measurements (together with the Geometric Phase Analysis, GPA, see Fig. S9 in Suppl. Mat.) therefore support the predictions of AIMD and CMD simulations, which indicate formation of B3-AlN domains in [110]-elongated SLs (Figs. 3 and Fig. 5b).

The reduction in out-of-plane TiN lattice spacings in the indented sample (compared d_{002}^{TiN} values in panel (f) and (b) of Fig. 7) can be ascribed to Poisson's contraction (following the increase of TiN lattice parameter in-plane) and to interface-induced Friedel oscillations [15]. Although no B4 phase was observed in the indented sample, cross-sectional HRTEM images reveal the presence of a monoclinic AlN phase (not shown), which is a transition state during the B1-to-B4 transformation [53]. Furthermore, we note that previous experimental investigations by Yalamanchili *et al.* [65] showed that strain-induced B1-to-B4 AlN transformation occurs in nanoindented nanoscale multilayers of $ZrN/Zr_{0.63}Al_{0.37}N$. Consistently with our predictions, the authors suggested that the transformation-associated volume expansion significantly improved fracture resistance of the films.

Fig. 8 further emphasises the similarities between simulation predictions and experimental observations. CMD results of SLs subject to [110] (in-plane) elongation show B1-to-B3 transformations—initiated by $\{111\}\langle 1\bar{1}0\rangle$ AlN slip—which lead to layer interpenetration and, ultimately, fracture along shear bands (Figs. 8a, 5b, and Suppl. Fig. S4 and Fig. S5). Analogously, HRTEM of nanoindented films evidences shear-mediated AlN↔TiN interpenetration and formation of diagonal cracks along slip lines (Fig. 8b). Additional STEM-HAADF data in Suppl. Mat. Fig. S11 show layer slipping/interpenetration and crack opening diagonally across the sample. Although similar to CMD theoretical predictions, dedicated experimental investigations will be needed to fully validate our interpretations of fracture mechanisms. The next step on the simulation side could be SL models with pre-existing cracks (see e.g. Ref. [66]), providing insights for the SL fracture toughness and supporting stress intensity factor (K) measurements.

3.5. CMD quantification of bilayer period effects

As indicated earlier, key atomic-level mechanisms that underlie plasticity and crack growth in AlN/TiN SLs are deformation-mediated phase transformations in AlN layers. "Large" CMD superlattice models allow to analyse these structural changes on a quantitative level. In Fig. 9, we plot relative portion of different AlN polymorph structures together with the average coordination of Al atoms as a function of strain during tensile elongation.

Subject to [001]-strain (Fig. 9a), up to 3, 9, 19, and 32% of AlN layers consist of the B4 phase in SLs with Λ of 1.25, 2.5, 5, and 10 nm, respectively. The transformation initiates when [001]-strain exceeds $\varepsilon \approx 8\%$ (i.e. 6% earlier compared to AIMD simulations, due to the smaller supercell size and the absence of Poisson's contraction in AIMD). After reaching a maximum at around 15%-[001] strain, the B4 volume fraction suddenly drops (for all Λ), as a consequence of SL fracture via cleavage (see Fig. 5a). The corresponding stress release facilitates the reverse B4-to-B1 transformation (reduction in purple colouring in Fig. 5a), thus, the B4 content decreases, which is mirrored by an increase of the average Al coordination number (bottom panel of Fig. 9b).

Compared to SLs loaded orthogonal to interfaces (Fig. 9a), their [110]-loaded counterparts (Fig. 9b) exhibit phase transformations to an even greater extent. Specifically, up to 12, 18, 32, and 44% of AlN transforms to the B3 phase in SLs with Λ of 1.25, 2.5, 5, and 10 nm, respectively. The strain at which the B3-AlN content reaches its maximum increases with increasing Λ. As suggested by analysing snapshots of AIMD and CMD simulations, AlN can form hybrid B3(B4)-like domains, indication of which is the decrease of the average Al coordination (to 4–5) in the bottom panel of Fig. 9(b), already at 4–5% strain, for which no fully transformed B3(B4) phase is detected.

Trends in structural changes induced by [100] loading (Fig. 9c) are less obvious, perhaps because our analysis does not include the B_k hexagonal phase, which predominantly forms in SLs with $\Lambda = 1.25$, 2.5 nm. The largest extent of the B1-to-B4 transformation is predicted for the SL with $\Lambda = 10$ nm followed by $\Lambda = 5$ nm, while SLs with $\Lambda = \{1.25, 2.5\}$ nm show lower content of the B4-AlN. Consistently with AIMD results, also CMD simulations indicate that nucleation of the B4-AlN in SLs subject to [100]-elongation requires relatively high tensile strains, above $\approx 13\%$, while only $\approx 8\%$ strain suffices for B1-to-B3(B4) transformation in case of [001] and [110] loading. However, the decrease of the mean Al coordination already at $\approx 4\%$ strain (bottom panel in Fig. 9) indicates nearly the same onset of structural changes (Al atoms being less than 6-folded), irrespective of the loading condition and bilayer period.

The results presented in previous sections point towards strong toughness dependence on the bilayer period. In particular, Fig. 5 suggests that the "sweet spot" is in the vicinity of $\Lambda \approx 2.5$ nm.

A decrease of Λ to 1.25 nm promotes formation of shear bands during [110] elongation, followed by nanocracking diagonally across interfaces (the left panel in Fig. 5b), while an increase of Λ to 5 and 10 nm largely accelerates void opening in TiN layers during [100] loading (right panels in Fig. 5c). To support this qualitative observation, we estimate bilayer period effect on SL toughness by introducing a toughness-indicator

$$I_{\mathrm{tough}} = \left(\prod_{i=1}^{n} U_T^i \right)^{\frac{1}{n}}, \tag{1}$$

as a geometric mean of the toughness moduli U_T^i calculated for ith elongation $[h_i k_i l_i]$. Analogically, the ideal strength, σ_T^i, is here used

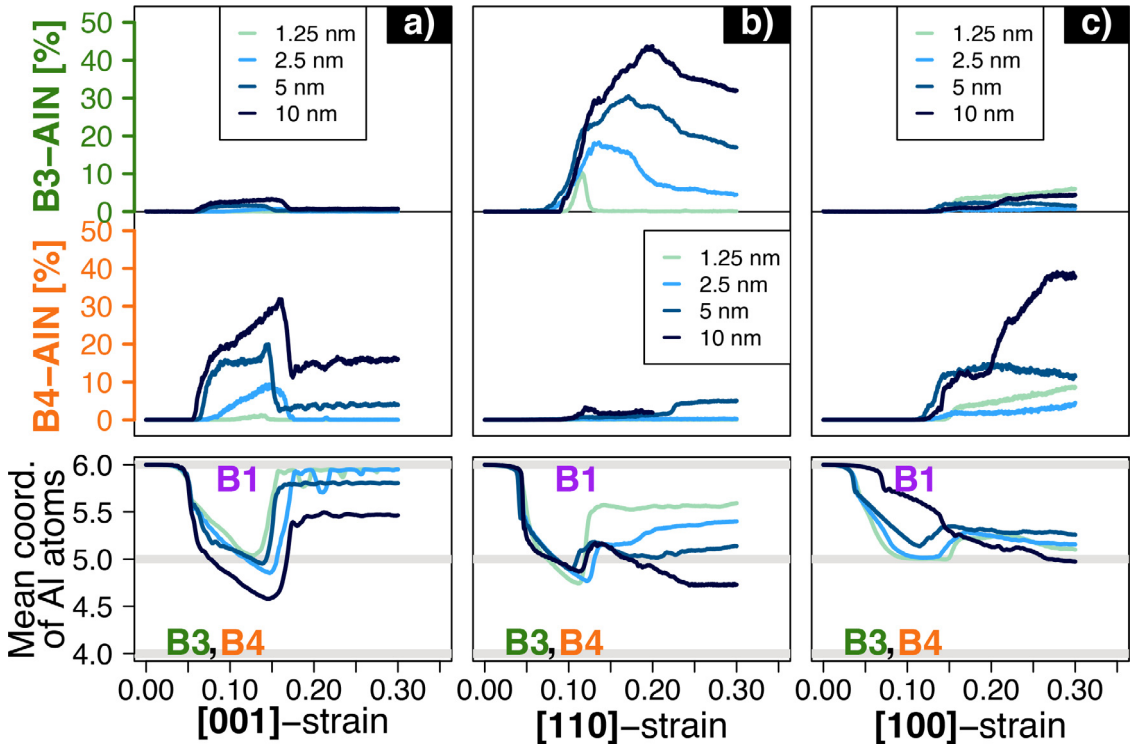

Fig. 9. CMD-calculated volume fractions of the B3-AlN (green y-axis) and B4-AlN (orange y-axis) in AlN/TiN SLs subject to tensile deformation in the (a) [001], (b) [110], and (c) [100] direction. Different shades of blue solid lines correspond to $\Lambda = \{1.25, 2.5, 5, 10\}$ nm. The bottom panels (a–c) depict the mean coordination number of Al atoms in the SL.

to introduce a strength-indicator

$$I_{\text{strength}} = \left(\prod_{i=1}^{n} \sigma_T^i \right)^{\frac{1}{n}} . \tag{2}$$

The in-plane I_{tough} and I_{strength} values are expected to relate with mechanical performance of SL-based protective coatings during use, as the compressive-stress induced by external load would be primarily accommodated via lateral deformation. In Fig. 10 and its inset, we plot the in-plane toughness and in-plane strength indicators, I_{tough} and I_{strength}, for which the products in Eqs. (1) and (2) run over $[h_1k_1l_1] = [110]$ and $[h_2k_2l_2] = [100]$. The underlying σ_T and U_T values, evaluated based on CMD stress/strain data, are listed in the Suppl. Mat. (Tab. S1). Fig. 10 suggests that AlN/TiN SL with $\Lambda = 2.5$ nm possesses superior strength and toughness to other SLs, hence support our previous considerations based on analysing SL snapshots during the simulated tensile tests. This observation would not be altered if $\sigma_T^{[001]}$ and $U_T^{[001]}$ values were also included in the products of Eqs. (1) and (2). Encouragingly, also experimental investigations by *Fallmann* et al. (see Fig. 3a in Ref. [14] but mind the variation of AlN-to-TiN volume fraction) demonstrate that hardness of AlN(001)/TiN(001) SL films increases with decreasing Λ, peaking for the lowest investigated $\Lambda = 2.5$ nm. For the same bilayer period, cube corner mechanical testing indicates the highest SL toughness.

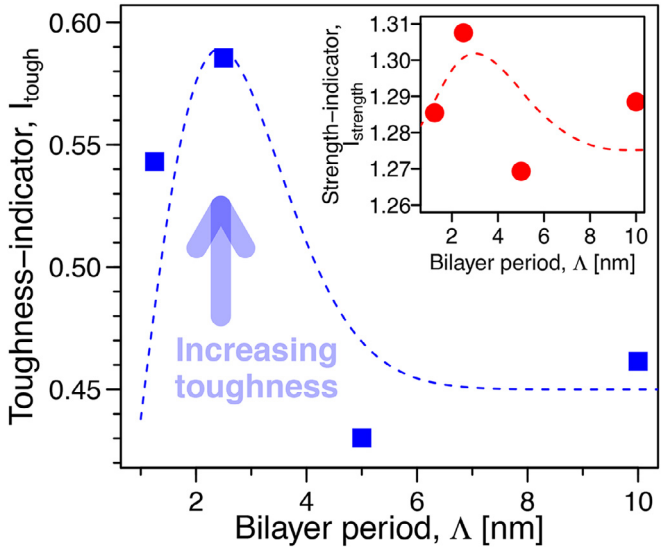

Fig. 10. CMD indicators of SL toughness I_{tough}, Eq. (1), and strength I_{strength}, Eq. (2), plotted on a $\log_{10}$ scale as a function of the bilayer period. The dashed lines (inspired by measured trends of hardness [8,9,67] and toughness [5,7,11] vs. Λ in nitride SLs) serve as guide to the eye.

Although additional simulations would be needed to gain statistical confidence of the evolution of mechanical properties with the bilayer period, superlattices with $\Lambda \approx 2.5$ nm—which enable *intermediate AlN transformations, rapidly extending to TiN layers with increasing in-plane strain*—seem close to optimum combination of strength and toughness (Fig. 10). Concerning the SL strength, it is established that relatively facile nucleation and motion of dislocations is detrimental for hardness. Slip-induced softening is typically attributed to SLs with "too low" (easy glide across interfaces) or "too high" (easy glide within layers) bilayer periods [9,10]. In our case, $\Lambda \approx 2.5$ nm impedes dislocation nucleation and motion within individual layers, while might also hinder slip across interfaces more effectively than lower Λ. The slightly higher tensile strengths predicted for the two lowest bilayer periods in Fig. 10 are underpinned by dislocation analysis (Suppl. Fig. S8), showing much lower dislocation densities (low total dislocation lengths) for SLs with $\Lambda = \{1.25, 2.5\}$ nm in comparison to $\Lambda = \{5, 10\}$ nm. Note that in the B3/B4-like domains, other slip

systems than those typical for B1 nitrides may be activated, increasing energetic costs of dislocation movement. Together with interfaces, transformed AlN domains also consume crack energy, i.e. contribute to SL toughness. Again, *intermediate* bilayer periods enable efficient stress dissipation—via strain-activated transformations across AlN and TiN layers—which delays crack nucleation and propagation.

4. Summary and conclusions

Tensile loading of cubic B1 AlN(001)/TiN(001) superlattices—with 1:1 AlN-to-TiN ratio and bilayer periods Λ ranging from 1.25 to 10 nm—was modelled using ab initio and classical molecular dynamics to gain atomic-level understanding of trends in plasticity and fracture resistance as a function of Λ.

The simulations showed strongly directional and bilayer-period-dependent mechanical responses:

- SLs loaded **orthogonal to interfaces** (along [001]) exhibited only modest plasticity and cleaved parallel to interfaces.
- SLs loaded **parallel to interfaces** (along [110] or [100]) showed superior plasticity (transformation-induced) and fracture resistance compared to [001]-strained SLs.
- Irrespective of Λ, SLs strained along in-plane [110] directions undergo local B1-to-B3 AlN transformations which eventually lead to shear-mediated layer interpenetration followed by fracture along shear bands.
- The fracture resistance of SLs strained along in-plane [100]-directions is observed to be strongly Λ-dependent. Relatively low bilayer periods (1.25-2.5 nm) enable strain-mediated lattice transformations which extend through the SL, thus dissipating accumulated stress and enhancing toughness. Relatively high bilayer periods (5-10 nm) undergo localised AlN transformations which increase interfacial strain with adjacent TiN layers, eventually causing crack nucleation and propagation.

HRTEM analyses of nanoindented AlN/TiN films supported our theoretical findings. For example, consistently with our predictions, formation of B3-AlN domains together with AlN/TiN layer slipping/interpenetration and nanocracking diagonally across interfaces were experimentally observed in B1-AlN(001)/TiN(001) SL coatings after nanoindentation orthogonal to interfaces (which locally induces in-plane tensile stresses).

The simulations predicted superior strength and toughness for AlN/TiN SLs with *intermediate* bilayer periods ($\Lambda \approx 2.5$ nm), which hinder plastic flow across interfaces at early deformation stages, while enabling intermediate AlN transformations that extend to TiN layers with increased load.

Declaration of Competing Interest

The authors declare that they have no known competing financial interests or personal relationships that could have appeared to influence the work reported in this paper.

Acknowledgments

NK acknowledges the DOC fellowship by the Austrian Academy of Sciences, ÖAW. LL, DH, ZC and ZZ highly appreciate the support by the Austrian Science Fund, FWF, (P 30341-N36, P 33696). DGS gratefully acknowledges financial support from the Competence Center Functional Nanoscale Materials (FunMat-II) (Vinnova Grant No. 2016-05156), the Swedish Research Council (VR) through Grant Nr. VR-2021-04426, and the Olle Engkvist Foundation. Computational resources were provided by the Vienna Scientific Cluster (VSC) and by the Swedish National Infrastructure for Computing (SNIC), partially funded by the Swedish Reserach Council through Grant Agreement Nr. VR-2015-04630, on the Clusters located at the National Supercomputer Centre (NSC) in Linköping, the Center for High Performance Computing (PDC) in Stockholm, and at the High Performance Computing Center North (HPC2N) in Umeå, Sweden.

Supplementary material

Supplementary material associated with this article can be found, in the online version, at doi:10.1016/j.actamat.2022.117809.

References

[1] Y. Chen, T. Guo, J. Wang, X. Pang, L. Qiao, Effects of orientation on microstructure and mechanical properties of TiN/AlN superlattice films, Scripta Materialia 201 (2021) 113951.
[2] S. Du, K. Zhang, M. Wen, P. Ren, Q. Meng, Y. Zhang, W. Zheng, Crystallization of SiC and its effects on microstructure, hardness and toughness in TaC/SiC multilayer films, Ceramics International 44 (1) (2018) 613–621.
[3] Z. Zhang, X. Gu, D. Holec, M. Bartosik, P.H. Mayrhofer, H.P. Duan, Superlattice-induced oscillations of interplanar distances and strain effects in the CrN/AlN system, Physical Review B 95 (15) (2017) 155305.
[4] N. Koutná, A. Brenner, D. Holec, P.H. Mayrhofer, High-throughput first-principles search for ceramic superlattices with improved ductility and fracture resistance, Acta Materialia 206 (2021) 116615.
[5] R. Hahn, N. Koutná, T. Wójcik, A. Davydok, S. Kolozsvári, C. Krywka, D. Holec, M. Bartosik, P.H. Mayrhofer, Mechanistic study of superlattice-enabled high toughness and hardness in MoN/TaN coatings, Communications Materials 1 (1) (2020) 1–11.
[6] Z. Zhang, Z. Chen, D. Holec, C.H. Liebscher, N. Koutná, M. Bartosik, Y. Zheng, G. Dehm, P.H. Mayrhofer, Mapping the mechanical properties in nitride coatings at the nanometer scale, Acta Materialia 194 (2020) 343–353.
[7] R. Hahn, M. Bartosik, R. Soler, C. Kirchlechner, G. Dehm, P.H. Mayrhofer, Superlattice effect for enhanced fracture toughness of hard coatings, Scripta Materialia 124 (2016) 67–70.
[8] U. Helmersson, S. Todorova, S.A. Barnett, J.-E. Sundgren, L.C. Markert, J.E. Greene, Growth of single-crystal TiN/VN strained-layer superlattices with extremely high mechanical hardness, J. Appl. Phys. 62 (2) (1987) 481–484.
[9] S. Barnett, A. Madan, Superhard superlattices, Physics world 11 (1) (1998) 45.
[10] X. Chu, S.A. Barnett, Model of superlattice yield stress and hardness enhancements, Journal of Applied Physics 77 (9) (1995) 4403–4411.
[11] J. Buchinger, N. Koutná, Z. Chen, Z. Zhang, P.H. Mayrhofer, D. Holec, M. Bartosik, Toughness enhancement in TiN/WN superlattice thin films, Acta Materialia 172 (2019) 18–29.
[12] J. Buchinger, A. Wagner, Z. Chen, Z. Zhang, D. Holec, P.H. Mayrhofer, M. Bartosik, Fracture toughness trends of modulus-matched TiN/(Cr, Al)N thin film superlattices, Acta Materialia 202 (2021) 376–386.
[13] A. Wagner, D. Holec, P.H. Mayrhofer, M. Bartosik, Enhanced fracture toughness in ceramic superlattice thin films: on the role of coherency stresses and misfit dislocations, Materials & Design 202 (2021) 109517.
[14] M. Fallmann, Z. Chen, Z.L. Zhang, P.H. Mayrhofer, M. Bartosik, Mechanical properties and epitaxial growth of TiN/AlN superlattices, Surface and Coatings Technology 375 (2019) 1–7.
[15] N. Koutná, P. Řehák, Z. Chen, M. Bartosik, M. Fallmann, M. Černỳ, Z. Zhang, M. Friák, M. Šob, P.H. Mayrhofer, D. Holec, Correlating structural and mechanical properties of AlN/TiN superlattice films, Scripta Materialia 165 (2019) 159–163.
[16] M.-S. Wong, G.-Y. Hsiao, S.-Y. Yang, Preparation and characterization of AlN/ZrN and AlN/TiN nanolaminate coatings, Surface and Coatings Technology 133 (2000) 160–165.
[17] Z. Li, S. Yadav, Y. Chen, N. Li, X.-Y. Liu, J. Wang, S. Zhang, J.K. Baldwin, A. Misra, N. Mara, Mechanically controlling the reversible phase transformation from zinc blende to wurtzite in AlN, Materials Research Letters 5 (6) (2017) 426–432.
[18] Z. Chen, D. Holec, M. Bartosik, P.H. Mayrhofer, Z. Zhang, Crystallographic orientation dependent maximum layer thickness of cubic AlN in CrN/AlN multilayers, Acta Materialia 168 (2019) 190–202.
[19] K. Kutschej, P.H. Mayrhofer, M. Kathrein, P. Polcik, R. Tessadri, C. Mitterer, Structure, mechanical and tribological properties of sputtered $Ti_{1-x}Al_xN$ coatings with $0.5 \leq x \leq 0.75$, Surface and Coatings Technology 200 (7) (2005) 2358–2365.
[20] D.G. Sangiovanni, F. Tasnadi, L.J.S. Johnson, M. Odén, I.A. Abrikosov, Strength, transformation toughening, and fracture dynamics of rocksalt-structure $Ti_{1-x}Al_xN$ ($0 \leq x \leq 0.75$) alloys, Physical Review Materials 4 (3) (2020) 033605.
[21] M. Meindlhumer, J. Zalesak, R. Pitonak, J. Todt, B. Sartory, M. Burghammer, A. Stark, N. Schell, R. Daniel, J. Keckes, Biomimetic hard and tough nanoceramic Ti–Al–N film with self-assembled six-level hierarchy, Nanoscale 11 (16) (2019) 7986–7995.
[22] F.F. Klimashin, H. Euchner, P.H. Mayrhofer, Computational and experimental studies on structure and mechanical properties of Mo–Al–N, Acta Materialia 107 (2016) 273–278.
[23] F. Anğay, L. Löfler, F. Tetard, D. Eyidi, P. Djemia, D. Holec, G. Abadias, Structure, stress, and mechanical properties of Mo-Al-N thin films deposited by dc reactive magnetron cosputtering: Role of point defects, Journal of Vacuum Science & Technology A: Vacuum, Surfaces, and Films 38 (5) (2020) 053401.

[24] F. Pacher, P.H. Mayrhofer, D. Holec, Vacancy-driven extended stability of cubic metastable Ta–Al–N and Nb–Al–N phases, Surface and Coatings Technology 326 (2017) 37–44.
[25] D. Holec, M. Friák, J. Neugebauer, P.H. Mayrhofer, Trends in the elastic response of binary early transition metal nitrides, Physical Review B 85 (6) (2012) 064101.
[26] J. Musil, M. Jirout, Toughness of hard nanostructured ceramic thin films, Surface and Coatings Technology 201 (9-11) (2007) 5148–5152.
[27] F.F. Klimashin, P.H. Mayrhofer, Ab initio-guided development of super-hard Mo–Al–Cr–N coatings, Scripta Materialia 140 (2017) 27–30.
[28] V. Moraes, L. Zauner, T. Wojcik, M. Arndt, P. Polcik, H. Riedl, P.H. Mayrhofer, Thermally stable superhard diborides: An ab initio guided case study for VW-diboride thin films, Acta Materialia 186 (2020) 487–493.
[29] M. Mikula, M. Truchlý, D.G. Sangiovanni, T. Plašienka D.and Roch, M. Gregor, P. Ďurina, M. Janík, P. Kúš, Experimental and computational studies on toughness enhancement in Ti-Al-Ta-N quaternaries, Journal of Vacuum Science & Technology A: Vacuum, Surfaces, and Films 35 (6) (2017) 060602.
[30] A. Madan, I.W. Kim, S.C. Cheng, P. Yashar, V.P. Dravid, S.A. Barnett, Stabilization of cubic AlN in epitaxial AlN/TiN superlattices, Physical Review Letters 78 (9) (1997) 1743.
[31] C. Stampfl, A.J. Freeman, Structure and stability of transition metal nitride interfaces from first-principles: AlN/VN, AlN/TiN, and VN/TiN, Applied surface science 258 (15) (2012) 5638–5645.
[32] G. Kresse, J. Furthmüller, Efficient iterative schemes for *ab initio*total-energy calculations using a plane-wave basis set, Physical Review B 54 (1996) 11169–11186.
[33] G. Kresse, D. Joubert, From ultrasoft pseudopotentials to the projector augmented-wave method, Physical Review B 59 (1999) 1758–1775.
[34] J.P. Perdew, K. Burke, M. Ernzerhof, Generalized Gradient Approximation Made Simple, Physical Review Letters 77 (1996) 3865–3868.
[35] D.G. Sangiovanni, Inherent toughness and fracture mechanisms of refractory transition-metal nitrides via density-functional molecular dynamics, Acta Materialia 151 (2018) 11–20.
[36] A.B. Mei, H. Kindlund, E. Broitman, L. Hultman, I. Petrov, J.E. Greene, D.G. Sangiovanni, Adaptive hard and tough mechanical response in single-crystal B1 VN_x ceramics via control of anion vacancies, Acta Materialia 192 (2020) 78–88.
[37] M. Parrinello, A. Rahman, Polymorphic transitions in single crystals: A new molecular dynamics method, Journal of Applied physics 52 (12) (1981) 7182–7190.
[38] S. Plimpton, Fast parallel algorithms for short-range molecular dynamics, J. Comput. Phys. 117 (1) (1995) 1–19.
[39] G.A. Almyras, D.G. Sangiovanni, K. Sarakinos, Semi-empirical force-field model for the $Ti_{1-x}Al_xN$ ($0 \leq x \leq 1$) system, Materials 12 (2) (2019) 215.
[40] A. Stukowski, Visualization and analysis of atomistic simulation data with ovito–the open visualization tool, Modelling and Simulation in Materials Science and Engineering 18 (1) (2009) 015012.
[41] E. Maras, O. Trushin, A. Stukowski, T. Ala-Nissila, H. Jonsson, Global transition path search for dislocation formation in Ge on Si (001), Computer Physics Communications 205 (2016) 13–21.
[42] A. Stukowski, V.V. Bulatov, A. Arsenlis, Automated identification and indexing of dislocations in crystal interfaces, Modelling and Simulation in Materials Science and Engineering 20 (8) (2012) 085007.
[43] Z. Chen, Y. Zheng, L. Löfler, M. Bartosik, G.K. Nayak, O. Renk, D. Holec, P.H. Mayrhofer, Z. Zhang, Atomic insights on intermixing of nanoscale nitride multilayer triggered by nanoindentation, Acta Materialia 214 (2021) 117004.
[44] S. Brinckmann, K. Matoy, C. Kirchlechner, G. Dehm, On the influence of microcantilever pre-crack geometries on the apparent fracture toughness of brittle materials, Acta Materialia 136 (2017) 281–287.
[45] K. Matoy, H. Schönherr, T. Detzel, T. Schöberl, R. Pippan, C. Motz, G. Dehm, A comparative micro-cantilever study of the mechanical behavior of silicon based passivation films, Thin Solid Films 518 (1) (2009) 247–256.
[46] P. Larsson, A.E. Giannakopoulos, Tensile stresses and their implication to cracking at pyramid indentation of pressure-sensitive hard metals and ceramics, Materials Science and Engineering: A 254 (1-2) (1998) 268–281.
[47] H. Wang, H. Zeng, Q. Li, J. Shen, Superlattice supertoughness of TiN/MN (M=V, Nb, Ta, Mo, and W): first-principles study, Thin Solid Films 607 (2016) 59–66.
[48] D. Pettifor, Theoretical predictions of structure and related properties of intermetallics, Materials Science and Technology 8 (1992) 345–349.
[49] P. Řehák, M. Černý, D. Holec, Interface-induced electronic structure toughening of nitride superlattices, Surface and Coatings Technology 325 (2017) 410–416.
[50] N. Farrer, L. Bellaiche, Properties of hexagonal ScN versus wurtzite GaN and InN, Physical Review B 66 (20) (2002) 201203.
[51] D. Holec, R. Franz, P.H. Mayrhofer, C. Mitterer, Structure and stability of phases within the NbN–AlN system, Journal of Physics D: Applied Physics 43 (14) (2010) 145403.
[52] R.F. Zhang, S.H. Sheng, S. Veprek, Mechanism of the B3 to B1 transformation in cubic AlN under uniaxial stress, Physical Review B 76 (7) (2007) 075208.
[53] R.F. Zhang, S. Veprek, Deformation paths and atomistic mechanism of B4→B1 phase transformation in aluminium nitride, Acta materialia 57 (7) (2009) 2259–2265.
[54] M. Odén, H. Ljungcrantz, L. Hultman, Characterization of the induced plastic zone in a single crystal TiN (001) film by nanoindentation and transmission electron microscopy, Journal of materials research 12 (8) (1997) 2134–2142.
[55] H. Ljungcrantz, M. Odén, L. Hultman, J.E. Greene, J.-E. Sundgren, Nanoindentation studies of single-crystal (001)-,(011)-, and (111)-oriented TiN layers on MgO, Journal of applied physics 80 (12) (1996) 6725–6733.
[56] C.-S. Shin, D. Gall, N. Hellgren, J. Patscheider, I. Petrov, J.E. Greene, Vacancy hardening in single-crystal TiN_x(001) layers, Journal of Applied Physics 93 (10) (2003) 6025–6028.
[57] Z. Xu, Z. Zhang, M. Bartosik, Y. Zhang, P.H. Mayrhofer, Y. He, Insight into the structural evolution during TiN film growth via atomic resolution TEM, Journal of Alloys and Compounds 754 (2018) 257–267.
[58] C. Mastail, M. David, F. Nita, A. Michel, G. Abadias, Ti, Al and N adatom adsorption and diffusion on rocksalt cubic AlN (001) and (011) surfaces: Ab initio calculations, Applied Surface Science 423 (2017) 354–364.
[59] S. Uehara, T. Masamoto, A. Onodera, M. Ueno, O. Shimomura, K. Takemura, Equation of state of the rocksalt phase of III–V nitrides to 72 GPa or higher, Journal of Physics and Chemistry of Solids 58 (12) (1997) 2093–2099.
[60] L.H. Shen, X.F. Li, Y.M. Ma, K.F. Yang, W.W. Lei, Q.L. Cui, G.T. Zou, Pressure-induced structural transition in aln nanowires, Applied physics letters 89 (14) (2006) 141903.
[61] Z. Zhang, A. Ghasemi, N. Koutná, Z. Xu, T. Grünstäudl, K. Song, D. Holec, Y. He, P.H. Mayrhofer, M. Bartosik, Correlating point defects with mechanical properties in nanocrystalline TiN thin films, Materials & Design (2021) 109844.
[62] A. Zeilinger, J. Todt, C. Krywka, M. Müller, W. Ecker, B. Sartory, M. Meindlhumer, M. Stefenelli, R. Daniel, C. Mitterer, J. Keckes, In-situ observation of cross-sectional microstructural changes and stress distributions in fracturing TiN thin film during nanoindentation, Scientific reports 6 (1) (2016) 1–14.
[63] J.H. Edgar, Properties of group III nitrides, Inst of Engineering & Technology, 1994.
[64] U. Verma, P. Bisht, Ab-initio study of AlN in zinc-blende and rock-salt phases, Solid state sciences 12 (5) (2010) 665–669.
[65] K. Yalamanchili, I.C. Schramm, E. Jiménez-Piqué, L. Rogström, F. Mücklich, M. Odén, N. Ghafoor, Tuning hardness and fracture resistance of $ZrN/Zr_{0.63}Al_{0.37}N$ nanoscale multilayers by stress-induced transformation toughening, Acta Materialia 89 (2015) 22–31.
[66] Y. Zeng, Q. Zhang, Y. Wang, J. Jiang, H. Xing, X. Li, Toughening and Crack Healing Mechanisms in Nanotwinned Diamond Composites with Various Polytypes, Physical Review Letters 127 (6) (2021) 066101.
[67] P. Mirkarimi, L. Hultman, S.A. Barnett, Enhanced hardness in lattice-matched single-crystal $TiN/VTiN/V_{0.6}Nb_{0.4}NNb_{0.4}N$ superlattices, Applied physics letters 57 (25) (1990) 2654–2656.